CRYSTAL GROWTH & DESIGN

pubs.acs.org/crystal

Article

Cation Dynamics as Structure Explorer in Hybrid Perovskites—The Case of $MAPbI_3$

Published as part of Crystal Growth & Design virtual special issue "Lattice Dynamics".

Kacper Drużbicki,* Pablo Gila-Herranz, Pelayo Marin-Villa, Mattia Gaboardi, Jeff Armstrong, and Felix Fernandez-Alonso*

Cite This: *Cryst. Growth Des.* 2024, 24, 391−404

Read Online

ACCESS | Metrics & More | Article Recommendations | Supporting Information

ABSTRACT: Hybrid organic−inorganic perovskites exhibit remarkable potential as cost-effective and high-efficiency materials for photovoltaic applications. Their exceptional chemical tunability opens further routes for optimizing their optical and electronic properties through structural engineering. Nevertheless, the extraordinary softness of the lattice, stemming from its interconnected organic−inorganic composition, unveils formidable challenges in structural characterization. Here, by focusing on the quintessential methylammonium lead triiodide, $MAPbI_3$, we combine first-principles modeling with high-resolution neutron scattering data to identify the key stationary points on its shallow potential energy landscape. This combined experimental and computational approach enables us to benchmark the performance of a collection of semilocal exchange−correlation functionals and to track the local distortions of the perovskite framework, hallmarked by the inelastic neutron scattering response of the organic cation. By conducting a thorough examination of structural distortions, we introduce the *IKUR-PVP-1* structural data set. This data set contains nine mechanically stable structural models, each manifesting a distinct vibrational response. *IKUR-PVP-1* constitutes a valuable resource for assessing thermal behavior in the low-temperature perovskite phase. In addition, it paves the way for the development of accurate force fields, enabling a comprehensive understanding of the interplay between the structure and dynamics in $MAPbI_3$ and related hybrid perovskites.

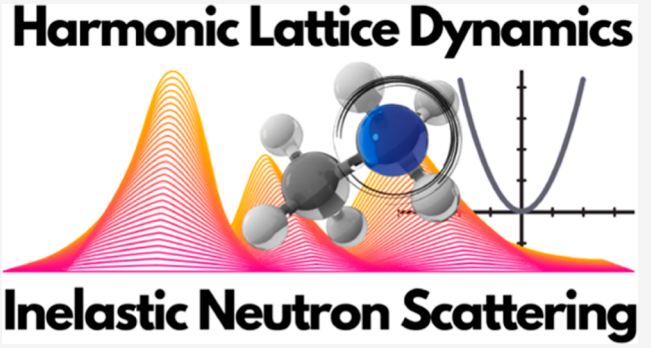

INTRODUCTION

Hybrid organic−inorganic perovskites (HOIPs) such as methylammonium lead triiodide ($MAPbI_3$) have recently attracted an enormous level of interest owing to their versatile applications in photovoltaics and photonics.[1] The crystal structure of three-dimensional (3D) HOIPs is characterized by a classic ABX_3 perovskite architecture, in which light and highly mobile organic cations are confined within the voids of the soft and heavy metal-halide framework. Such a duality translates into a coherent photocarrier transport characteristic of crystalline semiconductors, combined with a dielectric response and atomic dynamics reminiscent of those seen in liquids.[2] The extraordinary softness of the perovskite framework allows for exceptional chemical tunability, where different kinds of ions and/or their mixtures can be incorporated into the lattice. This key feature paves new routes for modifying electronic and optical properties, sensitive to the degree of orbital overlap dictated by the local structure of the material.[3−6]

The elucidation of the structure of inorganic perovskites poses significant challenges, and this task becomes even more complicated when dealing with HOIPs.[7−10] As a result of the shape anisotropy and charge distribution in nonspherical A-site cations, HOIPs have additional degrees of freedom compared to those of their all-inorganic analogues. Cations such as methylammonium (MA^+) show a propensity to donate protons and form hydrogen bonds with the neighboring halide ions, which can considerably affect the structure of the perovskite framework. Further, the subtle balance between complex dipole ordering and cation mobility in HOIPs usually reduces their crystal symmetry from cubic to tetragonal with decreasing temperature and, eventually, to cation-ordered orthorhombic phases. Depending on temperature and, therefore, on crystal structure, the A-site cations can be partly bound or move almost freely inside the cub-octahedral interstice. Yet,

Received: September 19, 2023
Revised: November 20, 2023
Accepted: December 1, 2023
Published: December 14, 2023

https://doi.org/10.1021/acs.cgd.3c01112
Cryst. Growth Des. 2024, 24, 391−404

the directional interactions arising from structural anisotropy can further alter this rich behavior, particularly at low temperatures. In fact, the space-group assignment of the prototypical $MAPbX_3$ (X = Cl, Br, and I) trihalides has not been devoid of controversy, and a similar situation is encountered when considering the evolution of the structure as a function of temperature. Notably, recurrent observation of nanoscale domains of different origins, mainly in scanning probe microscopy images, has led to a vivid debate about the ferroic properties of these materials.[4,11] A pronounced tendency to form nanoscale domains and superstructures, combined with a high propensity toward crystal twinning, further hampers a robust formulation of a comprehensive structural model bridging long-range and short-range order.[12,13]

As a result of the above, average crystal structures inferred from standard diffraction experiments often depart from the perovskite local structure, and a consistent picture of the short- and long-range structures remains a challenge to both experiment and computation.[14] This situation holds even within the "cation-ordered" phases observed at low temperatures, where the effects of dynamical disorder are minimized.[15] These limitations call for using local structure probes rather than conventional crystallographic techniques, the sensitivity of which is limited to long-range order. In this regard, nuclear magnetic resonance (NMR) and radiation-scattering techniques using photons and neutrons can be deployed.[15,16] In such a context, vibrational spectroscopy techniques, such as optical terahertz (THz) spectroscopy and inelastic neutron scattering (INS), can be considered valuable alternatives. THz spectroscopy combined with first-principles calculations allows insight into the local structure and the interactions responsible for preferred short-range ordering under temperature−pressure conditions that are often hardly accessible to other spectroscopy techniques. Figure 1 provides a visual summary illustrating the complementarity of the aforementioned techniques in discerning the low-energy vibrational response of $MAPbI_3$. INS is uniquely sensitive to the organic cation, given the large incoherent neutron cross section of hydrogen. In such a way, in our previous works, high-resolution INS and first-principles modeling have provided substantial evidence for the reduction of the local symmetry around the organic cation relative to the average in the low-temperature crystal structure of $MAPbI_3$.

Building upon our previous efforts,[15,19,21] this work systematically explores the low-temperature structural distortions in $MAPbI_3$. To this end, we developed a computational protocol accounting for all possible axial reorientations of the MA^+ cation in the low-temperature phase. Harmonic lattice dynamics (HLD) calculations utilizing a solid-state formulation of density functional theory (DFT) are used to explore the potential energy landscape. This exercise also provides a means of benchmarking modern semilocal density functional approximations (DFAs) and provides further insights into the local structure and preferable cation alignment in the low-temperature phase of $MAPbI_3$. We thoroughly scrutinize the large configuration space using high-resolution experimental INS data and identify a much-reduced subset of structural models with a systematically lowered crystallographic symmetry. This collection of structural models, hereafter denoted *IKUR-PVP-1*, was scrutinized further in terms of their thermodynamic and mechanical stability. Following a quantitative assessment of possible structural distortions at low temperatures, this data set also provides a new reference for further theoretical studies of $MAPbI_3$ and related HOIPs.

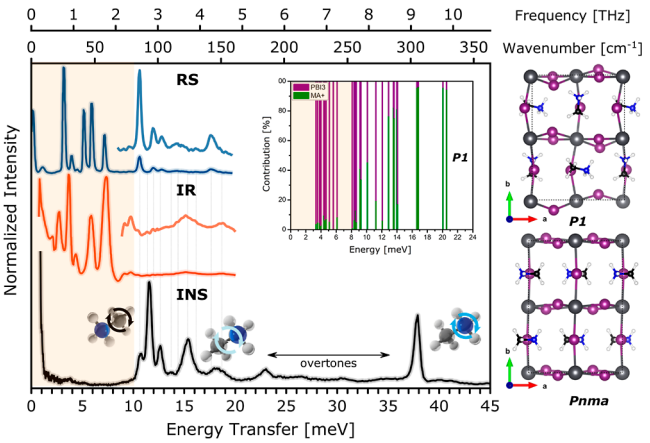

Figure 1. Comparison of low-frequency experimental Raman (RS, in blue),[17] infrared (IR, red),[18] and inelastic neutron scattering (INS, black) spectra of $MAPbI_3$.[17] These data have been obtained at low temperatures (4−20 K).[19] Optical spectra are also displayed in the 9−20 meV range to resolve the low-intensity features. Note the difference in the peak positions for each technique. The inset within the figure shows stacked histograms representing the contributions from the inorganic (PbI_3) and organic (MA^+) sublattices to the low-energy phonon modes, calculated using the *P1* model of the low-temperature phase.[17,20] The cartoons show characteristic cation vibrations linked to the most intense INS bands. Two alternative structural models of the low-temperature phase (*Pnma* and *P1*) are further presented on the right. The intense feature at ca. 40 meV is not accessible to the IR or Raman spectrum, and the most intense features in the optical spectra are solely linked to the inorganic framework. IR and Raman features exhibit a characteristic mutual exclusion arising from the centrosymmetric character of the structure of the low-temperature phase.

EXPERIMENTAL AND COMPUTATIONAL DETAILS

In situ neutron powder diffraction (NPD) measurements were performed on the OSIRIS backscattering instrument at the ISIS Neutron & Muon Spallation Source (STFC, Didcot, UK),[22−26] using the same hydrogenous sample of $MAPbI_3$ (purity >99%; Xi'an Polymer Light Technologies) that had been extensively characterized in our previous works.[15,21] Raw time-of-flight data were reduced to *d*-spacing using the Mantid software package,[27] roughly covering the range 3−6.5 Å. The whole pattern fitting of the NPD data was performed using the GSAS-ii software.[28] Instrument and profile parameters were fitted for a $Na_2Ca_3Al_2F_{14}$ (NaCaAlF) standard sample and fixed during the refinement of $MAPbI_3$.

The theoretical calculations were performed under periodic boundary conditions (PBCs) with the plane-wave pseudo-potential (PW-PP) formulation of DFT, as implemented in the CASTEP code.[29,30] The numerical settings, along with the selection of the semilocal DFAs, follow those used in our previous studies on $MAPbI_3$.[15,19,21,31] Following the work of Jepsen and Clark,[32] we emphasize the need for high numerical accuracy to achieve an accurate description of the potential energy surface (PES). In order to discern many closely lying local minima on a shallow potential energy landscape, the total energy was converged to within 1×10^{-12} eV/atom, which allowed us to minimize the residual atomic forces down to at least 1×10^{-5} eV/Å. These optimized trial models were further subjected to vibrational analysis using the finite-displacement method. The vibrational analysis allows us to confirm that the models are in mechanical equilibrium, *i.e.*, with all phonon modes having real and positive eigenvalues. The calculations of phonon band structures and related thermodynamic properties were performed with the non-

https://doi.org/10.1021/acs.cgd.3c01112
Cryst. Growth Des. 2024, 24, 391−404

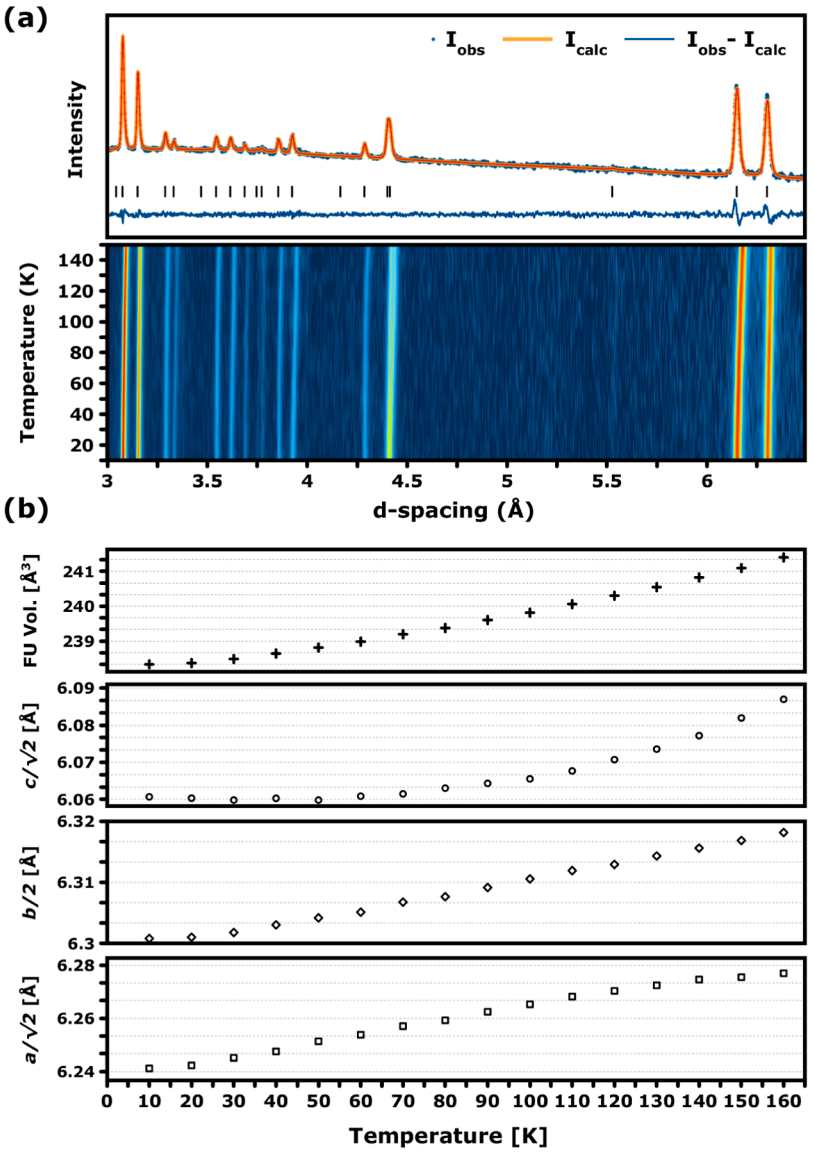

Figure 2. (a) Representative NPD pattern and associated whole−pattern profile refinement of $MAPbI_3$, collected at a base temperature of 10 K (top panel). The accompanying color map below shows the evolution of NPD intensities upon heating from the base temperature and across the stability regime of the low-temperature phase of $MAPbI_3$. (b) Pseudocubic cell parameters and volume in the low-temperature phase as a function of temperature. The adopted crystallographic convention follows the one presented earlier by Weller *et al.*[54] The cell volume is given per formula unit, and the orthorhombic cell parameters (a, b, and c) were converted to the pseudocubic ones using the following relations: $a/\sqrt{2}$, $b/2$, and $c/\sqrt{2}$.

diagonal supercell method of Lloyd-Williams and Monserrat to reduce the supercell size required to converge the dynamical matrix.[33] The phonon eigenvalues and eigenvectors calculated using HLD served as input for the further modeling of the INS spectra using the Abins and aClimax codes.[34,35] To further confirm the thermodynamic stability of the considered structures, we performed finite-temperature (50 K) AIMD simulations in the isothermal−isobaric (NpT) ensemble using the CP2K code,[36] following the Martyna−Tobias−Klein implementation,[37] and using the canonical sampling through the velocity rescaling (CSVR) thermostat to ensure the correct kinetic energy distribution.[37] Further computational details are provided in the Supporting Information.

RESULTS AND DISCUSSION

Neutron Scattering. Following the seminal work by Poglitsch and Weber,[38] a number of studies have explored the phase behavior of methylammonium lead halide triiodides ($MAPbX_3$, X = I, Br, and Cl) using X-ray and neutron diffraction for both powder and single-crystal specimens. These materials are commonly accepted to reveal three different crystal structures at ambient pressure, with increasing partial disorder upon heating a low-temperature cation-ordered phase; an intermediate tetragonal phase; and a high-temperature cubic phase. Yet, as extensively discussed in ref 39, no consensus has been reached on the space-group assignment, phase coexistence, or the formation of superstructures, particularly at low temperatures. In the case of $MAPbI_3$, the space-group assignment for both the low-temperature and ambient tetragonal phases has been debated from the outset. The low-temperature phase of $MAPbI_3$ was initially ascribed to a polar monoclinic $Pna2_1$[38] space group, which has been further refined by Baikie *et al.* to centrosymmetric orthorhombic $Pnma$[40] since the refinements and subsequent

https://doi.org/10.1021/acs.cgd.3c01112
Cryst. Growth Des. 2024, 24, 391−404

symmetry analyses were suggestive of missing symmetry elements in $Pna2_1$.[38] Notably, this work revealed the presence of some considerable residual electron density at distances unreasonably close to the iodine positions, possibly indicating short-range distortions of the corner-shared octahedra.[40] This assumption can be further inferred from subsequent neutron diffraction experiments,[41] suggesting the presence of considerable diffuse scattering even at cryogenic conditions, which seems to be related to the thermophysical and dielectric anomalies reported by Fabini and co-workers.[42] The analysis of the low-temperature (5 K) neutron pair distribution function (PDF) recorded for a perdeuterated d_6-$MAPbI_3$ also reveals some discrepancies when confronted with the *Pnma* model of the low-temperature structure.[41] The differences were found to be quite notable below r = 4 Å, attributable to close contacts between neighboring organic cations, and, hence, correlated with small structural fluctuations around MA^+.[41] Further controversies have focused on the structure of the ambient-temperature phase of $MAPbI_3$. Following a vibrant debate on the emergence of ferroic properties in $MAPbI_3$,[43] Breternitz *et al.*[44] have questioned the nonpolar *I*4/*mcm* assignment of the tetragonal phase in favor of a distorted *I*4*cm* structure—the maximal polar subgroup of the former. Yet, structural solutions in the polar *I*4*cm* structure have been unsuccessful, as reported elsewhere.[40,45−47] While focusing on cation disorder, differentiating unambiguously between the 4-fold and 8-fold disordered models is also challenging, even with high-quality neutron diffraction data,[41] calling for the use of subatomic resolution.[48] Likewise, the transition from the low-temperature to the tetragonal phase manifests a predominantly discontinuous character. Since no group-subgroup relationship exists between the *I*4/*mcm* and *Pnma* structures, it is impossible to descend continuously through this sequence.[40] As a consequence, the existence of an intermediate phase is justified for both $MAPbI_3$ and $MAPbBr_3$. The existence of such an intermediate phase has already been confirmed for the bromine analogue,[49,50] yet it has eluded clear experimental evidence for $MAPbI_3$. Despite revealing considerable contributions to the transition entropy already below 100 K, the thermophysical measurements could not resolve the presence of an intermediate state.[51] Yet, recent works report abnormal luminescent behavior around the tetragonal−orthorhombic phase transition,[52] as well as pronounced phase heterogeneity well within the range of orthorhombic-phase stability. These results raise additional questions about the existence of putative intermediate states over a broader range of temperatures and the extent of disorder in the low-temperature limit.[53]

To build a structural reference of the low-temperature phase of $MAPbI_3$, we performed variable-temperature NPD measurements, as presented in Figure 2. The NPD patterns could be indexed according to the *Pnma* model of the average structure provided by Weller *et al.*, as illustrated by the representative NPD pattern shown in Figure 2a.[54] The total profile refinement brought the average weighted-profile *R*-factor, R_{WP}, below 2% across the whole range of phase stability (Figure 2b). The associated structural parameters shown in this figure are in excellent agreement with the synchrotron X-ray diffraction data reported by Lehmann *et al.*[55] In line with this work, we also observed phase coexistence between 150 and 160 K upon heating. The total change in cell volume upon heating from 10 to 160 K was found to be below 1.5%. By inspecting the pseudocubic cell parameters, one can note a pronounced thermal expansion above 50 K. This trend is in line with the onset of enhanced cation dynamics observed in neutron-spectroscopic experiments.[56,57] These observations are in line with the substantial changes in local structure evinced from abnormal luminescent behavior at elevated temperatures, yet they do not seem to be so evident from the crystallographic lattice parameters.

Spectroscopic methods provide information about the local fluctuations of the structure at shorter time scales, which are subsequently smeared into a time-averaged scattered intensity. The experimental INS spectrum of $MAPbI_3$ is displayed in Figure 3a, reflecting the low-energy vibrational response of

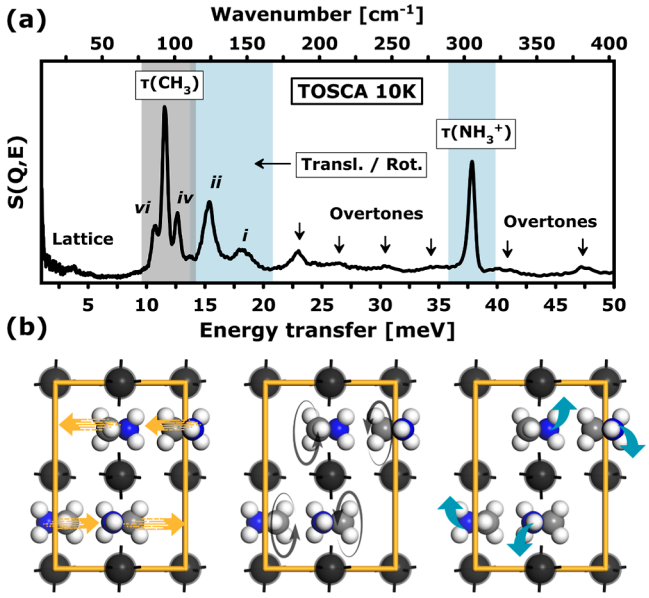

Figure 3. (a) Experimental INS spectrum of $MAPbI_3$ recorded at a base temperature of 10 K. The spectral range of 1−50 meV reflects the low-energy excitations of the MA^+ cation. The most intense features were ascribed to torsional modes localized on the NH_3^+ and CH_3 moieties. The librational transitions resulting from the coupling of translational and rotational motions are denoted by Roman numerals (*i*, *ii*, *iv*, and *vi*), following the previously established convention.[17] The spectral regions corresponding to vibrations predominantly localized on the NH_3^+ and CH_3 groups are represented by blue and gray color shading, respectively. (b) Schematic representation of the translational (left), internal torsional (middle), and external rotational motions (right) of the MA^+ cations. These motions contribute to the spectral range below 20 meV. For ease of visualization, the iodine atoms are omitted from the display.

MA^+. The cartoons displayed in Figure 3b schematically illustrate the rotational and translational character of the underlying vibrations, allowing for a generalized spectral interpretation of $MAPbI_3$ and related compounds. The key spectral features contribute at 38 meV [as $\tau(NH_3^+)$] and over the range of 10−20 meV. Following the convention introduced in previous works,[19] bands *i*−*ii* are ascribed to the MA^+ librations localized at the hydrogen-bonded (NH_3^+−C) moiety (see the cartoon at the bottom right side of Figure 3b). This set of three modes is expected to be highly sensitive to the strength of the confining potential according to interactions with the lead-halide cage. While INS spectroscopy is not subjected to optical selection rules, by further referring to optical THz spectra (see Figure 1), these librations are detectable by both IR and Raman spectroscopy, with spectral

https://doi.org/10.1021/acs.cgd.3c01112
Cryst. Growth Des. 2024, 24, 391−404

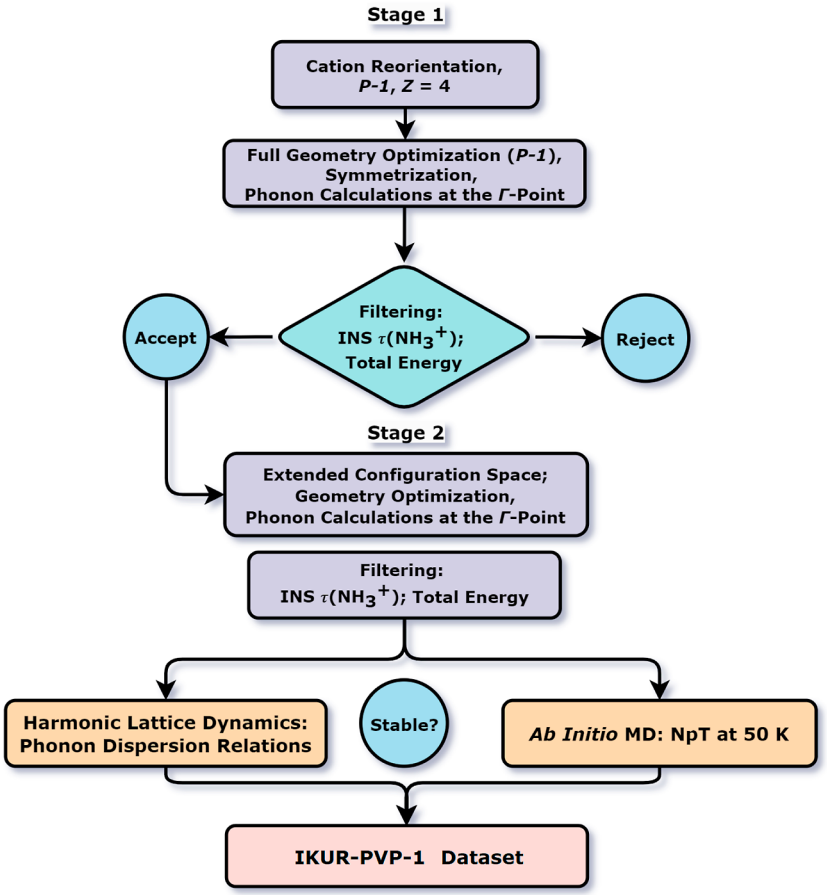

Figure 4. Schematic computational protocol established to systematically explore the configuration space in $MAPbI_3$ that results from cation reorientation. Stage 1 invokes systematic reorientation of the MA^+ cation in the centrosymmetric arrangement ($P\bar{1}$ symmetry constraint, $Z = 4$). This is followed by full cell relaxation and the subsequent synthesis of the resulting equilibrium structure. The phonon calculations at the Γ-point facilitate filtering of the generated ensemble in terms of total energy and degeneracy of the $\tau(NH_3^+)$ mode. In stage 2, the configuration space is expanded to incorporate previously reported models (ref 21) and those with $Z = 8$. Following subsequent geometry optimization and structure filtering, the stability of selected systems is confirmed through phonon dispersion relation calculations and *ab initio* MD simulations at 50 K. The fully mechanically stable structures are eventually gathered as the *IKUR-PVP-1* data set. See the main text for further details.

maxima at different energies. Similarly, the range below 10 meV shows high complementarity between IR and RS, which, according to the mutual exclusion rule, suggests the structure to be centrosymmetric. Analogously, the bands denoted as *iv* and *vi* reflect the similar librational character as *i* and *ii*, yet with an amplitude of displacement predominantly localized on the $(CH_3{-}N)$ fragments, yet with contributions of both cation rattling and the methyl-spinning mode, $\tau(CH_3^+)$, which has been schematically illustrated in Figure 3b. The spinning mode further defines the most intense spectral feature observed at ca. 12 meV. Interestingly, as in the case of $\tau(NH_3^+)$, this transition is silent in the optical spectra as it does not lead to a change of polarization or polarizability. We note that the well-resolved feature found at 11 meV in the RS spectrum is due to the libration denoted as *vi* in the INS spectrum.

Exploring the Configuration Space in $MAPbI_3$. Using the reference experimental data, we aim to explore the configuration space in $MAPbI_3$ by following axial reorientations of the MA^+ cation, dictating the dipole ordering in the low-temperature phase. To this end, we have developed a computational protocol that is presented in Figure 4. Our strategy combines a systematic exploration of the PES with HLD calculations, taking the experimental spectroscopic data as the reference. The computational protocol combines two stages, starting from different initial configurations. In stage I, the reference point stems from the aforementioned nonpolar *Pnma* model of the average structure reported by Weller *et al.*,[54] adopting the cell parameters obtained through the refinement of the OSIRIS data presented in the previous section. After scrutinizing the resulting configurations with respect to the experimental INS data, the configuration space has been further extended by accounting for the $Z = 8$ superstructures. The final set of structures presented as the *IKUR-PVP-1* data set was subjected to mechanical and thermodynamic stability analysis. We note that all of the total-energy considerations presented herein are given per $CH_3NH_3PbI_3$ formula unit.

Stage I: Search across Centrosymmetric Space ($Z = 4$). The starting point in our considerations was defining the rotational coordinates. This is analyzed in detail in Figure S1. Two rotational angles ϕ and θ define axial reorientations along the [110] and [101] directions in the standard crystallographic convention.[54] Since the *Pnma* structure involves eight symmetry elements, including the mirror plane perpendicular to the *y*-axis, which prevents ϕ rotations, the symmetry was lowered to $P\bar{1}$ leaving the inversion center as the only symmetry constraint. In the $Z = 4$ unit cell, there are two independent MA^+ cations, denoted as A and B, respectively. By

https://doi.org/10.1021/acs.cgd.3c01112
Cryst. Growth Des. 2024, 24, 391−404

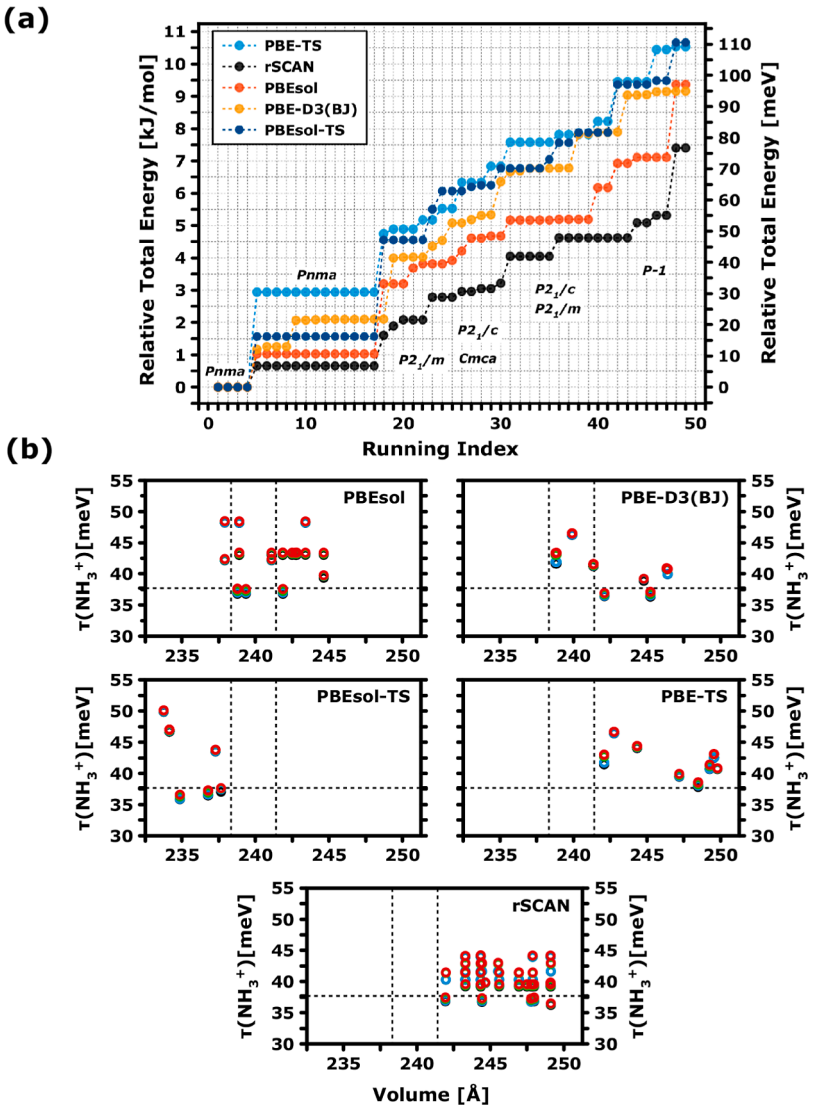

Figure 5. Benchmark of semilocal exchange−correlation functionals applied to the low-temperature phase of $MAPbI_3$. These results are obtained following the computational protocol outlined in Figure 4. (a) Relative total energies were examined as a function of different exchange−correlation functionals [PBEsol, rSCAN, PBEsol−TS, PBE−TS, and PBE−D3(BJ)]—concerning the lowest-energy model of *Pnma* symmetry. Symmetry labels highlight distinct structures resolved in a given energy range. (b) Energies of the τ (NH_3^+) disrotatory mode are examined as a function of the calculated volume for the set of unique energy structures identified in (a). The ensemble was subsequently refined based on the degeneracy of the resulting $\tau(NH_3^+)$ mode energies for the cations denoted as A (red) and B (blue), respectively. Dashed vertical lines denote the experimental volume boundaries, while the experimentally determined position of the $\tau(NH_3^+)$ band is indicated by a horizontal dashed line. For further details, see the main text.

combining rotations of 90° for each molecule, the configuration space explored in stage I contains forty-nine structures summarized in Table S1.

A reliable description of the shallow PES required high numerical precision, allowing for an accurate account of the underlying mechanical forces. Furthermore, the relative stability of the trial structures varying in shape and size was sensitive to the selection of the number of *k*-points in reciprocal space due to odd/even effects. As reported elsewhere, this issue is related to difficulties in describing the wave function phase factor at the center and boundaries of the Brillouin zone (BZ).[58] Thus, we carefully analyzed the energy convergence with respect to the density of the Monkhorst−Pack grid using the PBEsol functional. These results are presented in Figure S2, finding that a constant spacing of 0.05 Å, corresponding to the *k*-point mesh of 2 × 2 × 2, is required to converge the total energy within 1 kJ/mol and resolve the same number of distinct low-energy structures in the energy window of 1 kcal/mol. Afterward, we benchmarked semilocal DFA approximations for the whole configuration space, following the selection of exchange−correlation functionals presented in our previous works.[15,19,21] PBEsol with Tkatchenko−Scheffler corrections was included to check the performance of soft-GGA in conjunction with semiempirical dispersion corrections. The results of these tests are presented in Figure 5.

Exhaustive cell relaxation at ambient pressure allowed the minimization of the residual forces down to 1×10^{-5} eV/Å, and the resulting structures obtained at each level of theory were further symmetrized to the closest higher-symmetry space group, with a tolerance of 0.001 Å. The relative total energy as a function of different DFAs [PBEsol, rSCAN, PBEsol-TS,

https://doi.org/10.1021/acs.cgd.3c01112
Cryst. Growth Des. 2024, 24, 391−404

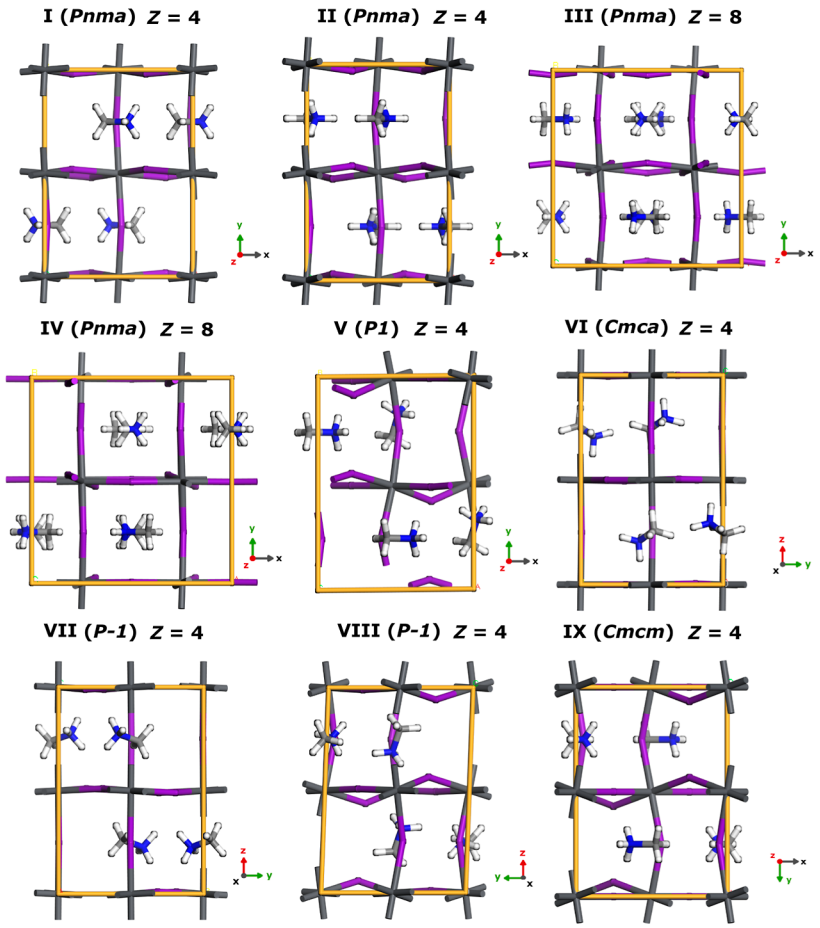

Figure 6. Collection of nine distinct structural models (I–IX) of the low-temperature phase of $MAPbI_3$ included in the *IKUR-PVP-1* data set. *Z* represents the number of asymmetric units per primitive unit cell of each model. The symmetry labels are given in parentheses. For ease of comparison, all of the models are aligned with the long crystal axis. The structural data set in the*.cif format is deposited in the Supporting Information.

PBE-TS, and PBE-D3(BJ)]—with respect to the lowest-energy model of *Pnma* symmetry is displayed in Figure 5a. The symmetry labels highlight distinct structures resolved in a given energy range for energetically distinct models. We note the significant influence of the exchange–correlation functional on the relative stability of each structure considered, with a significant contribution from dispersion corrections. The smallest relative differences were found for the rSCAN and PBEsol approximations, which severely miss the description of the van der Waals (vdW) forces yet are believed to provide an improved description of the inorganic framework. By comparing the two pairwise dispersion correction schemes, namely, TS and D3(BJ), the latter is augmented with the three-body term, and we note the energy difference at the order of 1 kJ/mol.

All the structures presented in Figure 5a were used to perform Γ-point phonon calculations, and the configuration space for each DFA was reduced by imposing the structure filtering in regard to the total energy and degeneracy of the $\tau(NH_3^+)$ spinning mode (see Figure 4). A relative total-energy threshold of 0.01 kJ/mol per formula unit was used to filter out clone structures. Since only a single band was resolved experimentally with INS, further analysis excluded models with pronounced site splitting, *i.e.*, all the structures varying in predicted $\tau(NH_3^+)$ energy by more than 1 meV. Band splitting was a common occurrence, particularly in the case of higher-energy $P2_1/m$ models. In Figure 5b, the reduced configuration space is analyzed as compared to the experimental limits in terms of the experimentally observed energy of the $\tau(NH_3^+)$ mode and the formula unit volume explored with NPD (see the horizontal and vertical dashed lines, respectively). For each functional but rSCAN, the number of distinct models was reduced by more than 70%, leaving about 10 distinct structures for further scrutiny. By inspection of Figure 5b, we note that only PBEsol and PBE-D3(BJ) provide structures commensurate with the cell volume observed experimentally. More advanced rSCAN and PBE-TS clearly overestimate the volumetric properties, and PBEsol-TS shows the opposite trend. While we anticipate that the inclusion of vdW-corrections might be beneficial for the future use of regularized SCAN functionals in HOIP simulations,[59] we further note issues with the use of TS corrections in the noniterative Hirshfeld partitioning scheme reported elsewhere.[60] This limitation also refers to the current implementation of the many-body dispersion (MBD) scheme in CASTEP, which has not been included in the analysis yet has been recommended elsewhere based on reference calculations using random phase approximation (RPA).[61] In line with our previous findings,[15] PBE-D3(BJ) has been considered the most advanced and versatile approximation for further analysis.

In Figure S3, the representative INS spectra obtained using PBE-D3(BJ) are compared to the ones calculated with PBEsol

https://doi.org/10.1021/acs.cgd.3c01112
Cryst. Growth Des. 2024, 24, 391–404

and rSCAN. At this stage, we note that the *Pnma* symmetry models by no means allow matching the experimental INS spectrum, with severe overestimation of the most intense spectral features due to the $\tau(NH_3^+)$ and $\tau(CH_3)$ spinning modes, and the considerably more advanced *meta*-GGA approximation represented by rSCAN does not provide a remedy in this regard. Yet, stage I provides a new, nonpolar model with *Cmca* symmetry, allowing a considerably improved description of the INS response. The *Cmca* symmetry was previously noted by Rakita *et al.* as an antiferroelectric analogue of the polar *I4 cm* model of the tetragonal phase of $MAPbI_3$, which shows antipolar displacements along the long cell axis.[11]

Stage II: Construction of the Structural Data Set. The *Cmca* model, developed in stage I, is among the highest symmetry models. Compared with *Pnma*, one of the screw axes transforms into a rotation axis. However, the structure with $Z = 4$ is primitive of a C-centered orthorhombic cell with $Z = 8$. This points to a possible scenario of cell doubling in the low-temperature phase of $MAPbI_3$. We note that to date, among the methylammonium lead trihalides, only $MAPbCl_3$ was found to show the low-temperature *Pnma* phase with $Z = 8$.[62] Motivated by this finding, we extended the configuration space to include $Z = 8$ superstructures. This type of superstructure corresponds to that used by Swainson for the case of $MAPbCl_3$. It is also based on the *Cmca* model introduced in the previous section by considering further axial reorientations of MA^+. In addition, the considered structural ensemble was augmented with the set of alternative models earlier reported by our group according to PBE-TS calculations.[21] In total, at stage II, we have further introduced 16 distinct models that are mechanically stable at the Γ-point as confirmed by the vibrational analysis. Once filtered against the $\tau(NH_3^+)$ site-splitting and total energy difference, the HLD calculations resolved 12 distinct models with no mechanical instabilities in the phonon band structure. Three of them were further rejected based on *NpT* MD simulations at 50 K as they rapidly relaxed (within 10 ps) to the nearest configuration with lower energy. Finally, the configuration space was reduced to nine configurations, which, according to AIMD simulations, can be considered the stationary points on the free energy surface (FES). These nine structures constitute the *IKUR-PVP-1* data set and are presented in Figure 6 sorted in terms of ascending total energy.

According to Figure 6, the four lowest-energy models (I–IV) are described by *Pnma* space-group symmetry. The common feature of the remaining models is the loss of the end-to-end cation ordering owing to uniaxial fluctuations of the MA^+ cations. Such structural distortions are challenging to be tackled by Bragg diffraction experiments, as discussed in detail with an example of the single-crystal studies of the tetragonal phase of $MAPbI_3$.[41] For example, in the tetragonal phase with *I*4/*mcm* symmetry, the cation could be disordered end-to-end, distributed over eight orientations in the unit cell or with the molecular axes aligned in an ordered manner, with only four accessible orientations. Using subatomic resolution single crystal neutron diffraction, Ren *et al.* have proposed an alternative disorder for the MA^+ cations, where nitrogen atoms remain ordered on the mirror plane and the methyl group is disordered off the mirror plane.[41,48] A similar scenario can be postulated for the low-temperature phase, yet its detailed description would be far more challenging.

A more thorough scrutiny of the local structure is given in Figure S4. The *P*1 model, introduced as a result of our previous efforts,[21] can be further symmetrized (within 0.1 Å tolerance) to the monoclinic *Cc* space group. In this case, the minimal cell is the primitive of the C-centered monoclinic phase with $Z = 2$, characterized by only two symmetry operators: identity and a glide plane (see Figure S4a). Similarly, the $P\bar{1}$ model, shown in Figure S4b, can be symmetrized to nearly isoenergetic configurations, *i.e.*, the monoclinic *C*2/*m* and the orthorhombic *Cmca*, commensurate in size with both primitive ($Z = 4$) and conventional cells ($Z = 8$) and preserving the mirror-plane as symmetry operator. Also, the monoclinic configurations are of possibly maximal symmetry for the higher energy models (see Figure S4c).

All the structures contained in the *IKUR-PVP-1* data set are subjected to thermodynamic analysis using the harmonic phonon calculations presented in Figure S5. At a given temperature T and constant pressure p, a material under interest reaches equilibrium by minimizing its Gibbs free energy[63]

$$G(T) = U(T) + pV - T[S(T)] \tag{1}$$

where $U(T)$ is the internal energy and $S(T)$ denotes the entropy term (which consists of both vibrational, $S_{vib}(T)$, and configurational, $S_{config}(T)$, contributions).[64]

Within the harmonic approximation, the Gibbs free energy of an electrical insulator as a function of temperature at a given pressure can be written as

$$G(T) = E_{latt.} + E_{vib.}(T) + pV - T[S(T)] \tag{2}$$

where the internal energy comprises both the $E_{latt.}$ and $E_{vib}(T)$ terms. $E_{latt.}$ is the ground-state lattice energy at 0 K, while $E_{vib}(T)$ is the total (thermal and zero-point vibrational energy). The pressure–volume work term, pV, is negligible at ambient pressure.[65,66] At constant volume, eq 2 can be rewritten to express the Helmholtz free energy, $F(T)$

$$F(T) = E_{latt.} + E_{vib.}(T) - T[S(T)] = E(T) - T[S(T)] \tag{3}$$

where $E(T)$ stands for the internal energy.

For a system consisting of a set of independent vibrational modes, the calculated phonon band structure encodes the harmonic energy $E_{q,j}$ of a given mode j at a given wave-vector branch q. The vibrational density of states [VDoS, $D(E)$], defined as the number of modes per unit of energy, is obtained by integrating over all q-points.[15] Using the VDOS, the thermodynamic quantities under interest can be expressed as follows[67]

$$F_{vib}(T) = k_B T \int_0^\infty \log\left[2\sinh\left(\frac{E}{2k_B T}\right)\right] D(E)\mathrm{d}E \tag{4}$$

$$E_{vib}(T) = \int_0^\infty \frac{E}{2}\coth\left(\frac{E}{2k_B T}\right) D(E)\mathrm{d}E \tag{5}$$

$$S_{vib}(T) = \frac{E_{vib} - F_{vib}}{T} \tag{6}$$

where k_B is Boltzmann's constant. In that sense, at the zero-temperature limit, the primary vibrational contributions stem from high-energy modes (see Figure S5a), whereas the thermal population above the ground vibrational state is driven mainly by low-energy modes (see Figure S5b).

https://doi.org/10.1021/acs.cgd.3c01112
Cryst. Growth Des. 2024, 24, 391–404

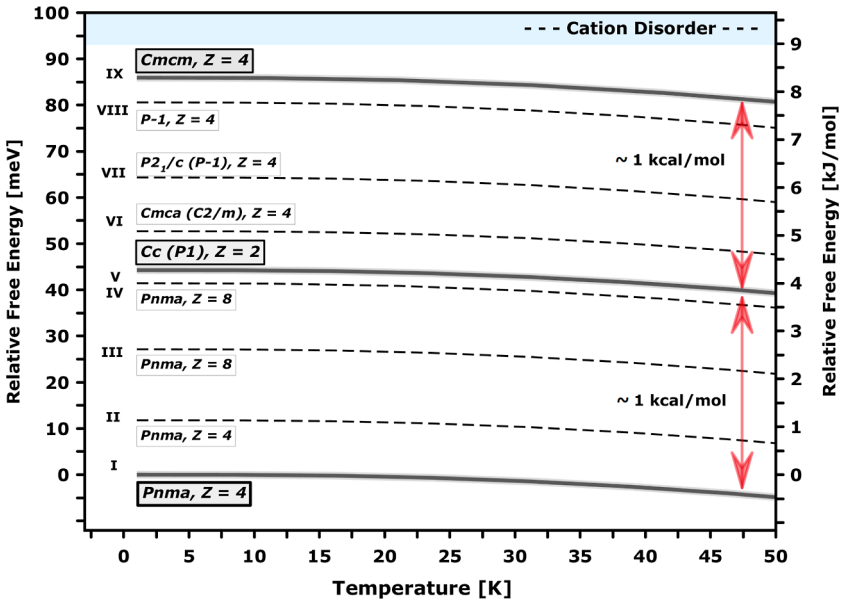

Figure 7. Thermodynamic properties of the low-temperature phase of $MAPbI_3$ in the low-temperature regime (<50 K) according to nine structural models (I–IX) collected as the *IKUR-PVP-1* data set. The results are obtained according to PBE-D3(BJ). The temperature-dependent harmonic Helmholtz free energy (F) for the lowest-energy *Pnma* structure and the intermediate *Cc* (*P1*) and *Cmcm* states are presented with solid lines, while the results for the remaining structures are depicted as black dashed lines. The energy contributions are expressed per formula unit basis and compared to the lowest-energy reference model denoted as I (*Pnma*).

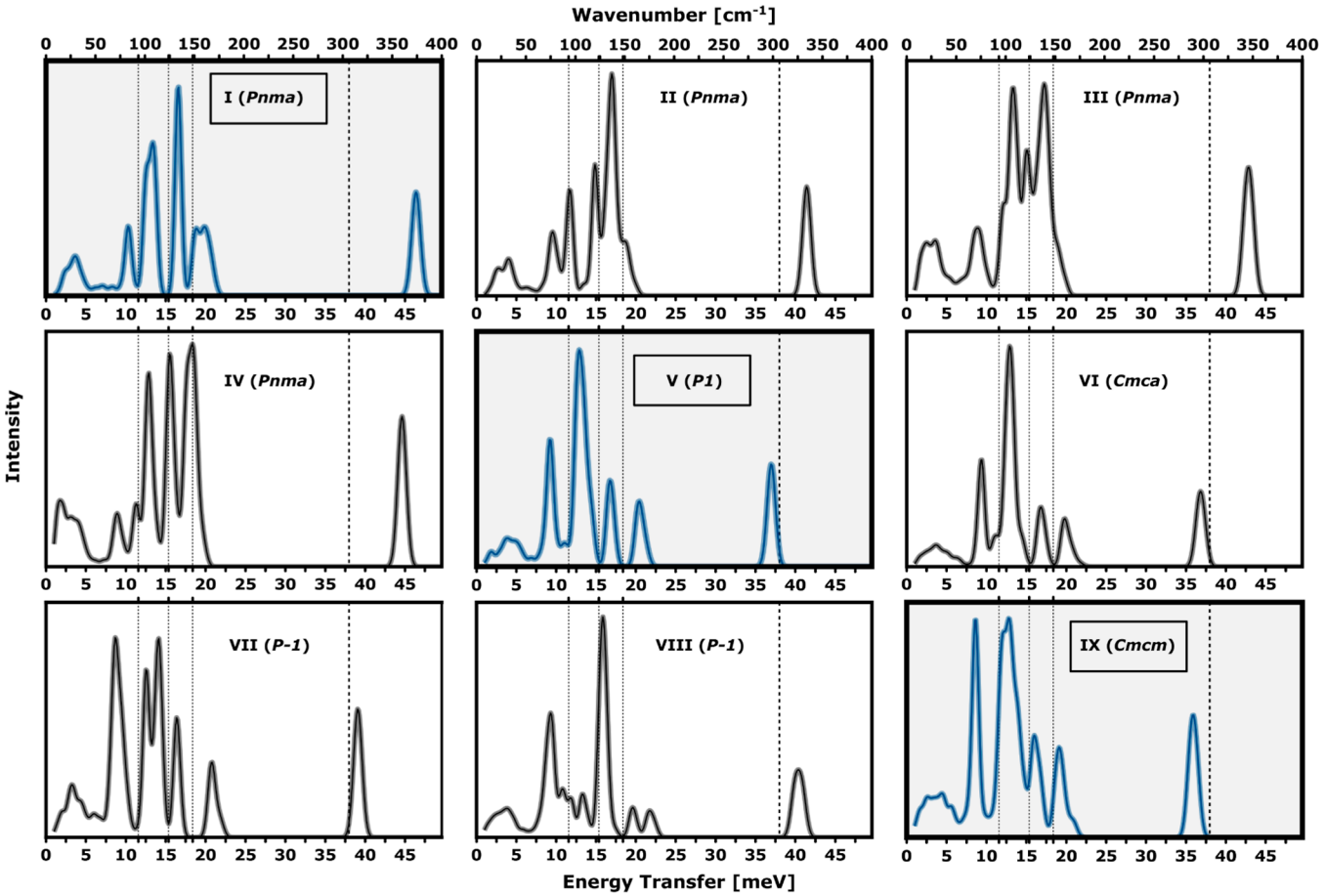

Figure 8. Theoretical INS spectra of the low-temperature phase of $MAPbI_3$ according to nine (I–IX) structural models comprising the *IKUR-PVP-1* data set. The spectral intensities are normalized with respect to the $\tau(NH_3^+)$ peak intensity. Dashed vertical lines denote the position of the most prominent bands observed experimentally at the base temperature. The spectral intensities were predicted from the set of PBE-D3(BJ) calculations using q-resolved harmonic phonon calculations across the first BZ. Only fundamental, one-phonon excitations were considered in the simulations.

https://doi.org/10.1021/acs.cgd.3c01112
Cryst. Growth Des. 2024, 24, 391−404

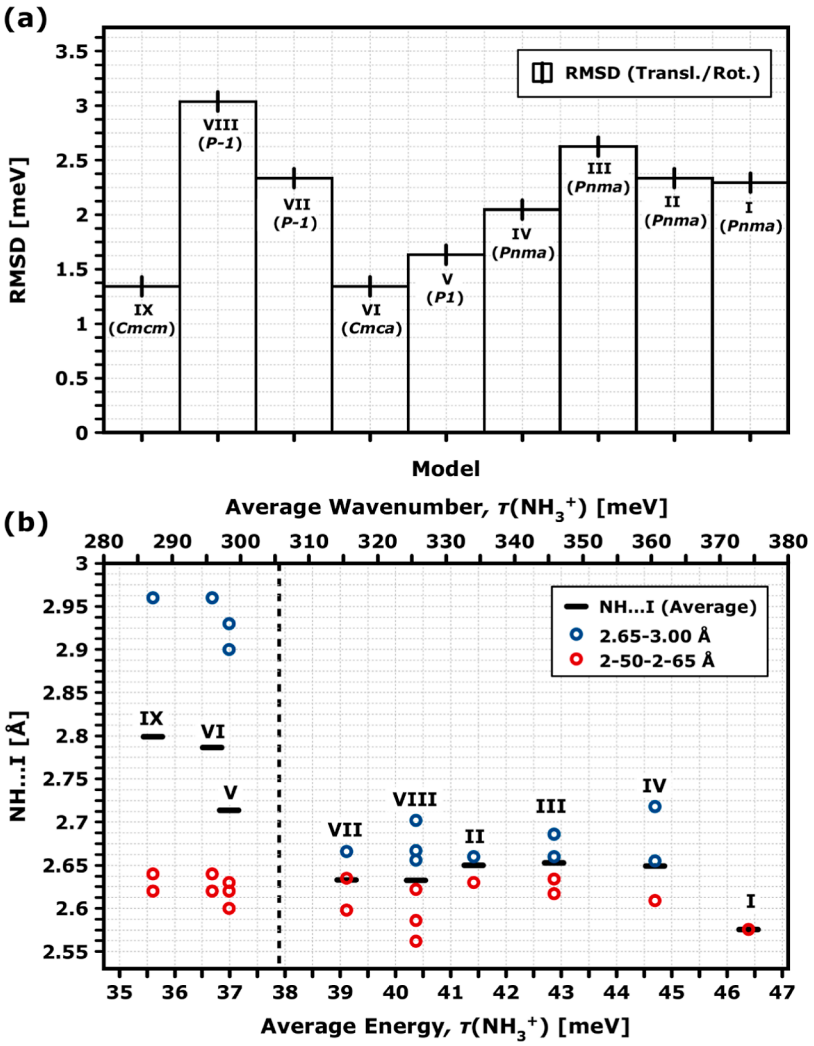

Figure 9. Quantitative analysis of the key vibrational and structural features for the nine structural models (I−IX) comprising the *IKUR-PVP-1* data set. (a) RMSDs for the predicted translational/rotational transitions. RMSD errors are calculated across the 5−25 meV range, considering the bands marked as *i*, *vi*, and $\tau(CH_3)$ in Figure 8. (b) Distribution of the NH···I contacts (2.50−3.00 Å) as a function of predicted $\tau(NH_3^+)$ mode energy. The close contacts below and beyond 2.70 Å are marked in red and blue, respectively. The energy of the $\tau(NH_3^+)$ band observed experimentally is marked with a dashed vertical line.

The analysis of structure stability obtained from HLD calculations is presented in Figure 7. In line with the phonon picture presented in Figure S5a, the 0 K vibrational contributions do not noticeably affect the energy difference between the considered models, generally contributing at the level of a fraction of kJ/mol per formula unit.

The differences at 0 K are mainly due to the electronic structure, and they are smaller than 100 meV, which is below the bending/stretching range of the phonon spectrum (see Figure S5a). At this point, we further recall the benchmark of DFAs presented in Figure 6, which shows that the difference in electronic energies can vary as much as 50% between different approximations. This finding calls for more advanced electronic structure calculations such as those using the RPA.[61,68] According to PBE-D3(BJ), the relative difference in free energy between the ground *Pnma* structure and the lowest-lying symmetry-lowered *P1* configuration[21] is below 1 kcal/mol, therefore below the chemical accuracy limit, which is hardly expected to be reachable with any of the DFAs tested in this work. Interestingly, this value roughly corresponds to the energy limit for the low-lying phonon band structure presented in Figure S5b.

Finally, Figure 8 compares the theoretical INS spectra obtained *via* phonon calculations beyond the Γ-point, sorted in terms of the increasing total energy. The dashed vertical lines represent the positions of key spectral features observed experimentally. A quantitative inspection of the root-mean-square deviation (RMSD) errors for the predicted translational/rotational transitions is further given in Figure 9a. Inspection of Figure 8 shows that all *Pnma* models (I−IV), including the ones with $Z = 8$ (III−IV), severely fail in the description of both $\tau(NH_3^+)$ and $\tau(CH_3)$ energies. The symmetry-lowering in structures V−IX significantly improves this picture, with both *P1* (V) and *Cmca* (VI) structures providing a much-improved description of the INS response in terms of both peak positions and spectral intensities across the whole spectral range of interest. As the RMSD analysis corroborates, these models also provide the most accurate descriptions of the key translational and rotational features across 7.5−25 meV.

https://doi.org/10.1021/acs.cgd.3c01112
Cryst. Growth Des. 2024, 24, 391−404

In addition, we refer to Figure 8b to correlate the MA−PbI_6 interactions with the spectral response. This panel shows the distribution of the NH···I contacts as a function of the average energy of the $\tau(NH_3^+)$ spinning mode. The symmetry of the ground-state *Pnma* configuration represents an extreme case where each donated proton participates in an equidistant NH···I contact of 2.58 Å. While giving rise to the strongest hydrogen-bonding interactions, INS spectroscopy does not support such a configuration. On the contrary, spatial fluctuations around the organic cation can considerably weaken the NH···I contacts with the inorganic framework. As such, the underlying NH···I distances for a given NH_3^+ fragment can differ by as much as 0.3 Å. This is the case for models *P1*(V), *Cmca*(VI), and *Cmcm*(IX), which provide the best match to INS data. The inequivalence of proton donation, resulting in double rather than triple hydrogen bonding, supports the spectroscopic picture with a substantial reduction of the RMSDs (see Figure 9a).

The local structure is further scrutinized according to Figures S7 and S8, providing a quantitative assessment of structural distortions around the organic moieties for the most representative models. As illustrated in Figure S8, the axial cation fluctuations are accompanied by the precession of the PbI_6 octahedra, as also seen in differences in the rotational angles ϕ, θ, and Ψ. Interestingly, the reduced tilting along some principal directions—*i.e.*, the 15° reduction of the [110] in-plane octahedral tilting (θ)—correlates with the presence of residual electron density in low-temperature X-ray diffraction data.[40] These axial fluctuations are accompanied by a 10° octahedral precession (ϕ and Ψ) out of the putative mirror plane.

CONCLUSIONS

Following up on our previous efforts in scrutinizing local structural distortions in $MAPbI_3$, we provide further spectroscopic insights into the low-temperature phase of $MAPbI_3$ at the limit of numerically precise HLD calculations. A new computational protocol was developed to explore possible structural distortions induced by the axial reorientation of anisotropic organic moieties in hybrid perovskites. As such, it represents an alternative for other well-established computational protocols, including the analysis of zone-boundary phonon instabilities.[69]

We find that cation fluctuations about the putative mirror-plane symmetry are a key feature to understand the distinct spectroscopic response of $MAPbI_3$ at low temperatures. The systematic computational screening with the help of solid-state DFT calculations allows resolving nine mechanically stable structures and the *IKUR-PVP-1* data set. This data set serves as a further guide to understanding the thermal evolution of the low-temperature phase, which could help address nagging questions on the origin of anomalies in the vicinity of the transition to the dynamically disordered phases of $MAPbI_3$.

By benchmarking several widely used semilocal DFT approximations, we pose further questions on their accuracy and the importance of the vdW corrections on the relative stabilization of energetically competing structures.[59,70,71] This further calls for using more advanced computational strategies to account for many-body electronic interactions.[61,68] Within the limits of the HLD approximation, this work also aims at stimulating more advanced analyses of the low-temperature phase of $MAPbI_3$ and related HOIPs, particularly in terms of the importance of anharmonicity nuclear quantum effects (NQEs).[72−76] Recent literature findings point at the importance of NQEs, which could affect quite considerably the angular velocity of the cation, further promoting the loss of the long-range end-to-end cation ordering.[77] We anticipate that the provided data set will facilitate the development of accurate force fields, allowing us to address these urgent questions with state-of-the-art computational strategies.[78−82]

Finally, the structures presented in this work could facilitate further understanding of the uncharted regimes of structural stability of $MAPbI_3$ and related HOIPs. This applies to the onset of orientational disorder at both extreme thermodynamic conditions and upon chemical stress introduced by cation engineering,[83] which continue to be a matter of vibrant debate.[84,85]

ASSOCIATED CONTENT

Supporting Information

The Supporting Information is available free of charge at https://pubs.acs.org/doi/10.1021/acs.cgd.3c01112.

Experimental and computational details; additional computational results; possible cation rotations considered within the initial data set; benchmark of regular *k*-point grid used in DFT calculations; theoretical INS spectra; structural transformation upon symmetrization of selected structural models; phonon band structure; results of NpT AIMD simulations; schematic representation of rotational angles describing cation orientations; close contacts and structural distortions in the representative models (PDF)

IKUR-PVP-1 data set (ZIP)

AUTHOR INFORMATION

Corresponding Authors

Kacper Drużbicki − *Materials Physics Center, CSIC-UPV/EHU, Donostia-San Sebastian 20018, Spain; Polish Academy of Sciences, Centre of Molecular and Macromolecular Studies, Lodz 90-363, Poland;* orcid.org/0000-0003-1759-2105; Email: kacper.druzbicki@ehu.eus

Felix Fernandez-Alonso − *Materials Physics Center, CSIC-UPV/EHU, Donostia-San Sebastian 20018, Spain; Donostia International Physics Center (DIPC), Donostia-San Sebastian 20018, Spain; IKERBASQUE, Basque Foundation for Science, Bilbao 48009, Spain;* orcid.org/0000-0003-0313-017X; Email: felix.fernandez@ehu.eus

Authors

Pablo Gila-Herranz − *Materials Physics Center, CSIC-UPV/EHU, Donostia-San Sebastian 20018, Spain*

Pelayo Marin-Villa − *Materials Physics Center, CSIC-UPV/EHU, Donostia-San Sebastian 20018, Spain;* orcid.org/0000-0001-5600-9600

Mattia Gaboardi − *Materials Physics Center, CSIC-UPV/EHU, Donostia-San Sebastian 20018, Spain; C.S.G.I. & Chemistry Department, University of Pavia, Pavia 27100, Italy*

Jeff Armstrong − *ISIS Neutron and Muon Facility, Rutherford Appleton Laboratory, Didcot OX11 0QX, U.K.;* orcid.org/0000-0002-8326-3097

Complete contact information is available at: https://pubs.acs.org/10.1021/acs.cgd.3c01112

https://doi.org/10.1021/acs.cgd.3c01112
Cryst. Growth Des. 2024, 24, 391−404

Notes

The authors declare no competing financial interest.

■ ACKNOWLEDGMENTS

The authors thank Prof. Michael T. Ruggiero (University of Vermont) for his invitation to write this contribution. The authors gratefully acknowledge the Science & Technology Facilities Council for access to beamtime at the ISIS Facility (Experiment RB1920012, DOI: 10.5286/ISIS.E.RB1920012-1). Financial support from the Spanish Ministry of Science and Innovation (grant PID2020-114506GB-100 funded by MCIN/AEI/10.13039/501100011033) and the Basque government (grant PIBA-2021-0026) is gratefully acknowledged. Grant PRE2021-097712 to support P.M.V. has been funded by MCIN/AEI/10.13039/501100011033 and the European Social Fund Programme "Investing in Your Future". We acknowledge generous HPC resources from PL-Grid Infrastructure (grant IDs: plghybrids; plghybrids2022; and plghybrids2023). We further acknowledge the Spanish Supercomputing Network (RES Activity: QHS-2023-1-0027) and the computational resources from the Donostia International Physics Center (DIPC; Atlas Facility). M.G. wishes to thank Chiara Milanese (University of Pavia) for the support. We gratefully acknowledge the financial support received from the IKUR Strategy under the collaboration agreement between the Ikerbasque Foundation and the Materials Physics Center, on behalf of the Department of Education of the Basque government.

■ REFERENCES

(1) Gonzalez-Pedro, V.; Juarez-Perez, E. J.; Arsyad, W.-S.; Barea, E. M.; Fabregat-Santiago, F.; Mora-Sero, I.; Bisquert, J. General Working Principles of $CH_3NH_3PbX_3$ Perovskite Solar Cells. *Nano Lett.* **2014**, *14*, 888−893.

(2) Miyata, K.; Atallah, T. L.; Zhu, X. Y. Lead Halide Perovskites: Crystal-liquid Duality, Phonon Glass Electron Crystals, and Large Polaron Formation. *Sci. Adv.* **2017**, *3*, 1−11.

(3) Mozur, E. M.; Maughan, A. E.; Cheng, Y.; Huq, A.; Jalarvo, N.; Daemen, L. L.; Neilson, J. R. Orientational Glass Formation in Substituted Hybrid Perovskites. *Chem. Mater.* **2017**, *29*, 10168−10177.

(4) Ambrosio, F.; De Angelis, F.; Goñi, A. R. The Ferroelectric−Ferroelastic Debate about Metal Halide Perovskites. *J. Phys. Chem. Lett.* **2022**, *13*, 7731−7740.

(5) McLeod, J. A.; Wu, Z.; Sun, B.; Liu, L. The Influence of the I/Cl Ratio on the Performance of $CH_3NH_3PbI_{3-x}Cl_x$−based Solar Cells: Why is CH_3NH_3I: $PbCl_2$ = 3:1 the "Magic" Ratio? *Nanoscale* **2016**, *8*, 6361−6368.

(6) Walsh, A. Principles of Chemical Bonding and Band Gap Engineering in Hybrid Organic−Inorganic Halide Perovskites. *J. Phys. Chem. C* **2015**, *119*, 5755−5760.

(7) Adams, D. J.; Churakov, S. V. Classification of Perovskite Structural Types with Dynamical Octahedral Tilting. *IUCrJ* **2023**, *10*, 309−320.

(8) Beecher, A. N.; Semonin, O. E.; Skelton, J. M.; Frost, J. M.; Terban, M. W.; Zhai, H.; Alatas, A.; Owen, J. S.; Walsh, A.; Billinge, S. J. L. Direct Observation of Dynamic Symmetry Breaking above Room Temperature in Methylammonium Lead Iodide Perovskite. *ACS Energy Lett.* **2016**, *1*, 880−887.

(9) Frost, J. M.; Walsh, A. What Is Moving in Hybrid Halide Perovskite Solar Cells? *Acc. Chem. Res.* **2016**, *49*, 528−535.

(10) Weadock, N. J.; Sterling, T. C.; Vigil, J. A.; Gold-Parker, A.; Smith, I. C.; Ahammed, B.; Krogstad, M. J.; Ye, F.; Voneshen, D.; Gehring, P. M.; et al. The Nature of Dynamic Local Order in $CH_3NH_3PbI_3$ and $CH_3NH_3PbBr_3$. *Joule* **2023**, *7*, 1051−1066.

(11) Rakita, Y.; Bar-Elli, O.; Meirzadeh, E.; Kaslasi, H.; Peleg, Y.; Hodes, G.; Lubomirsky, I.; Oron, D.; Ehre, D.; Cahen, D. Tetragonal $CH_3NH_3PbI_3$ is Ferroelectric. *Proc. Natl. Acad. Sci. U.S.A.* **2017**, *114*, E5504−E5512.

(12) Breternitz, J.; Tovar, M.; Schorr, S. Twinning in $MAPbI_3$ at Room Temperature Uncovered Through Laue Neutron Diffraction. *Sci. Rep.* **2020**, *10*, 16613−16618.

(13) Li, B.; Kawakita, Y.; Liu, Y.; Wang, M.; Matsuura, M.; Shibata, K.; Ohira-Kawamura, S.; Yamada, T.; Lin, S.; Nakajima, K.; Liu, S. F. Polar Rotor Scattering as Atomic-level Origin of Low Mobility and Thermal Conductivity of Perovskite $CH_3NH_3PbI_3$. *Nat. Commun.* **2017**, *8*, 16086−16089.

(14) Whalley, L. D.; Frost, J. M.; Jung, Y.-K.; Walsh, A. Perspective: Theory and Simulation of Hybrid Halide Perovskites. *J. Chem. Phys.* **2017**, *146*, 22090−22111.

(15) Marín-Villa, P.; Arauzo, A.; Drużbicki, K.; Fernandez-Alonso, F. Unraveling the Ordered Phase of the Quintessential Hybrid Perovskite $MAPbI_3$—Thermophysics to the Rescue. *J. Phys. Chem. Lett.* **2022**, *13*, 8422−8428.

(16) Kubicki, D. J.; Prochowicz, D.; Hofstetter, A.; Péchy, P.; Zakeeruddin, S. M.; Grätzel, M.; Emsley, L. Cation Dynamics in Mixed-Cation $(MA)_x(FA)_{1-x}PbI_3$ Hybrid Perovskites from Solid-State NMR. *J. Am. Chem. Soc.* **2017**, *139*, 10055−10061.

(17) Pérez-Osorio, M. A.; Milot, R. L.; Filip, M. R.; Patel, J. B.; Herz, L. M.; Johnston, M. B.; Giustino, F. Vibrational Properties of the Organic−Inorganic Halide Perovskite $CH_3NH_3PbI_3$ from Theory and Experiment: Factor Group Analysis, First-Principles Calculations, and Low-Temperature Infrared Spectra. *J. Phys. Chem. C* **2015**, *119*, 25703−25718.

(18) Pérez-Osorio, M. A.; Lin, Q.; Phillips, R. T.; Milot, R. L.; Herz, L. M.; Johnston, M. B.; Giustino, F. Raman Spectrum of the Organic−Inorganic Halide Perovskite $CH_3NH_3PbI_3$ from First Principles and High-Resolution Low-Temperature Raman Measurements. *J. Phys. Chem. C* **2018**, *122*, 21703−21717.

(19) Drużbicki, K.; Lavén, R.; Armstrong, J.; Malavasi, L.; Fernandez-Alonso, F.; Karlsson, M. Cation Dynamics and Structural Stabilization in Formamidinium Lead Iodide Perovskites. *J. Phys. Chem. Lett.* **2021**, *12*, 3503−3508.

(20) Kendrick, J.; Burnett, A. D. PDielec: The Calculation of Infrared and Terahertz Absorption for Powdered Crystals. *J. Comput. Chem.* **2016**, *37*, 1491−1504.

(21) Drużbicki, K.; Pinna, R. S.; Rudić, S.; Jura, M.; Gorini, G.; Fernandez-Alonso, F. Unexpected Cation Dynamics in the Low-temperature Phase of Methylammonium Lead Iodide: the Need for Improved Models. *J. Phys. Chem. Lett.* **2016**, *7*, 4701−4709.

(22) Demmel, F.; McPhail, D.; French, C.; Maxwell, D.; Harrison, S.; Boxall, J.; Rhodes, N.; Mukhopadhyay, S.; Silverwood, I.; Sakai, V. G.; Fernandez-Alonso, F. ToF-Backscattering Spectroscopy at the ISIS Facility: Status and Perspectives. *J. Phys.: Conf. Ser.* **2018**, *1021*, 012027.

(23) Telling, M. T. F.; Campbell, S. I.; Engberg, D.; Martín y Marero, D.; Andersen, K. H. Correction: Spectroscopic Characteristics of the OSIRIS Near-backscattering Crystal Analyser Spectrometer on the ISIS Pulsed Neutron Source. *Phys. Chem. Chem. Phys.* **2016**, *18*, 8243.

(24) Demmel, F.; McPhail, D.; Crawford, J.; Maxwell, D.; Pokhilchuk, K.; Garcia-Sakai, V.; Mukhopadyay, S.; Telling, M.; Bermejo, F.; Skipper, N.; Fernandez-Alonso, F. Opening the Terahertz Window on the OSIRIS Spectrometer. *EPJ Web Conf.* **2015**, *83*, 03003−03004.

(25) Telling, M. T. F.; Andersen, K. H. Spectroscopic Characteristics of the OSIRIS Near-backscattering Crystal Analyser Spectrometer on the ISIS Pulsed Neutron Source. *Phys. Chem. Chem. Phys.* **2005**, *7*, 1255−1261.

(26) Demmel, F.; Perrichon, A.; McPhail, D.; Luna Dapica, P.; Webb, N.; Cook, A.; Schooneveld, E.; Boxall, J.; Rhodes, N.; Lockett, C.; et al. Silver Jubilee for the OSIRIS Spectrometer: Achievements and Outlook. *EPJ Web Conf.* **2023**, *286*, 03005.

https://doi.org/10.1021/acs.cgd.3c01112
Cryst. Growth Des. 2024, 24, 391−404

(27) Arnold, O.; Bilheux, J.; Borreguero, J.; Buts, A.; Campbell, S.; Chapon, L.; Doucet, M.; Draper, N.; Ferraz Leal, R.; Gigg, M.; et al. Mantid-Data Analysis and Visualization Package for Neutron Scattering and μSR Experiments. *Nucl. Instrum. Methods Phys. Res.* **2014**, *764*, 156−166.
(28) Toby, B. H.; Von Dreele, R. B. GSAS-II: The Genesis of a Modern Open-source all Purpose Crystallography Software Package. *J. Appl. Crystallogr.* **2013**, *46*, 544−549.
(29) Payne, M. C.; Teter, M. P.; Allan, D. C.; Arias, T.; Joannopoulos, J. D. Iterative Minimization Techniques for Ab Initio Total-energy Calculations—Molecular-Dynamics and Conjugate Gradients. *Rev. Mod. Phys.* **1992**, *64*, 1045−1097.
(30) Clark, S. J.; Segall, M. D.; Pickard, C. J.; Hasnip, P. J.; Probert, M. I. J.; Refson, K.; Payne, M. C. First Principles Methods Using CASTEP. *Z. Kristallogr.* **2005**, *220*, 567−570.
(31) Drużbicki, K.; Gaboardi, M.; Fernandez-Alonso, F. Dynamics & Spectroscopy with Neutrons-Recent Developments & Emerging Opportunities. *Polymers* **2021**, *13*, 1440−1444.
(32) Jepsen, P. U.; Clark, S. J. Precise Ab-initio Prediction of Terahertz Vibrational Modes in Crystalline Systems. *Chem. Phys. Lett.* **2007**, *442*, 275−280.
(33) Lloyd-Williams, J. H.; Monserrat, B. Lattice Dynamics and Electron-phonon Coupling Calculations Using Nondiagonal Supercells. *Phys. Rev. B* **2015**, *92*, 184301−184309.
(34) Dymkowski, K.; Parker, S. F.; Fernandez-Alonso, F.; Mukhopadhyay, S. AbINS: The Modern Software for INS Interpretation. *Phys. B* **2018**, *551*, 443−448.
(35) Cheng, Y. Q.; Daemen, L. L.; Kolesnikov, A. I.; Ramirez-Cuesta, A. J. Simulation of Inelastic Neutron Scattering Spectra Using OCLIMAX. *J. Chem. Theory Comput.* **2019**, *15*, 1974−1982.
(36) Kühne, T. D.; Iannuzzi, M.; Del Ben, M.; Rybkin, V. V.; Seewald, P.; Stein, F.; Laino, T.; Khaliullin, R. Z.; Schütt, O.; Schiffmann, F.; et al. CP2K: An Electronic Structure and Molecular Dynamics Software Package-Quickstep: Efficient and Accurate Electronic Structure Calculations. *J. Chem. Phys.* **2020**, *152*, 194103−194147.
(37) Martyna, G. J.; Tobias, D. J.; Klein, M. L. Constant Pressure Molecular Dynamics Algorithms. *J. Chem. Phys.* **1994**, *101*, 4177−4189.
(38) Poglitsch, A.; Weber, D. Dynamic Disorder in Methylammoniumtrihalogenoplumbates (II) Observed by Millimeter-wave Spectroscopy. *J. Chem. Phys.* **1987**, *87*, 6373−6378.
(39) López, C. A.; Alvarez-Galván, M. C.; Abia, C.; Fernández-Díaz, M. T.; Alonso, J. A. *Perovskite and Piezoelectric Materials*; IntechOpen, 2021.
(40) Baikie, T.; Fang, Y.; Kadro, J. M.; Schreyer, M.; Wei, F.; Mhaisalkar, S. G.; Graetzel, M.; White, T. J. Synthesis and Crystal Chemistry of the Hybrid Perovskite $(CH_3NH_3)PbI_3$ for Solid-State Sensitised Solar Cell Applications. *J. Mater. Chem. A* **2013**, *1*, 5628−5641.
(41) Whitfield, P. S.; Herron, N.; Guise, W. E.; Page, K.; Cheng, Y. Q.; Milas, I.; Crawford, M. K. Structures, Phase Transitions and Tricritical Behavior of the Hybrid Perovskite Methyl Ammonium Lead Iodide. *Sci. Rep.* **2016**, *6*, 35685−35716.
(42) Fabini, D. H.; Hogan, T.; Evans, H. A.; Stoumpos, C. C.; Kanatzidis, M. G.; Seshadri, R. Dielectric and Thermodynamic Signatures of Low-Temperature Glassy Dynamics in the Hybrid Perovskites $CH_3NH_3PbI_3$ and $HC(NH_3)_3PbI_3$. *J. Phys. Chem. Lett.* **2016**, *7*, 376−381.
(43) Rakita, Y.; Bar-Elli, O.; Meirzadeh, E.; Kaslasi, H.; Peleg, Y.; Hodes, G.; Lubomirsky, I.; Oron, D.; Ehre, D.; Cahen, D. Tetragonal $CH_3NH_3PbI_3$ is Ferroelectric. *Proc. Natl. Acad. Sci. U.S.A.* **2017**, *114*, E5504−E5512.
(44) Breternitz, J.; Lehmann, F.; Barnett, S. A.; Nowell, H.; Schorr, S. Role of the Iodide Methylammonium Interaction in the Ferroelectricity of $CH_3NH_3PbI_3$. *Angew. Chem., Int. Ed.* **2020**, *59*, 424−428.
(45) Szafrański, M.; Katrusiak, A. Photovoltaic Hybrid Perovskites under Pressure. *J. Phys. Chem. Lett.* **2017**, *8*, 2496−2506.
(46) Onoda-Yamamuro, N.; Matsuo, T.; Suga, H. Dielectric Study of $CH_3NH_3PbX_3$ (X = Cl, Br, I). *J. Phys. Chem. Solids* **1992**, *53*, 935−939.
(47) Frohna, K.; Deshpande, T.; Harter, J.; Peng, W.; Barker, B. A.; Neaton, J. B.; Louie, S. G.; Bakr, O. M.; Hsieh, D.; Bernardi, M. Inversion Symmetry and Bulk Rashba Effect in Methylammonium Lead Iodide Perovskite Single Crystals. *Nat. Commun.* **2018**, *9*, 1829.
(48) Ren, Y.; Oswald, I. W. H.; Wang, X.; McCandless, G. T.; Chan, J. Y. Orientation of Organic Cations in Hybrid Inorganic−Organic Perovskite $CH_3NH_3PbI_3$ from Subatomic Resolution Single Crystal Neutron Diffraction Structural Studies. *Cryst. Growth Des.* **2016**, *16*, 2945−2951.
(49) Wiedemann, D.; Breternitz, J.; Paley, D. W.; Schorr, S. Hybrid Perovskite at Full Tilt: Structure and Symmetry Relations of the Incommensurately Modulated Phase of Methylammonium Lead Bromide, $MAPbBr_3$. *J. Phys. Chem. Lett.* **2021**, *12*, 2358−2362.
(50) Abia, C.; López, C. A.; Cañadillas-Delgado, L.; Fernández-Diaz, M. T.; Alonso, J. A. Crystal Structure Thermal Evolution and Novel Orthorhombic Phase of Methylammonium Lead Bromide, $CH_3NH_3PbBr_3$. *Sci. Rep.* **2022**, *12*, 18647.
(51) Onoda-Yamamuro, N.; Matsuo, T.; Suga, H. Calorimetric and IR Spectroscopic Studies of Phase Transitions in Methylammonium Trihalogenoplumbates (II). *J. Phys. Chem. Solids* **1990**, *51*, 1383−1395.
(52) Kong, W.; Ye, Z.; Qi, Z.; Zhang, B.; Wang, M.; Rahimi-Iman, A.; Wu, H. Characterization of an Abnormal Photoluminescence Behavior upon Crystal-phase Transition of Perovskite $CH_3NH_3PbI_3$. *Phys. Chem. Chem. Phys.* **2015**, *17*, 16405−16411.
(53) Stavrakas, C.; Zelewski, S. J.; Frohna, K.; Booker, E. P.; Galkowski, K.; Ji, K.; Ruggeri, E.; Mackowski, S.; Kudrawiec, R.; Plochocka, P.; et al. Influence of Grain Size on Phase Transitions in Halide Perovskite Films. *Adv. Energy Mater.* **2019**, *9*, 1901883−1901887.
(54) Weller, M. T.; Weber, O. J.; Henry, P. F.; Di Pumpo, A. M.; Hansen, T. C. Complete Structure and Cation Orientation in the Perovskite Photovoltaic Methylammonium Lead Iodide Between 100 and 352 K. *Chem. Commun.* **2015**, *51*, 4180−4183.
(55) Lehmann, F.; Franz, A.; Többens, D.; Levcenco, S.; Unold, T.; Taubert, A.; Schorr, S. The Phase Diagram of a Mixed Halide (Br, I) Hybrid Perovskite Obtained by Synchrotron X-ray Diffraction. *RSC Adv.* **2019**, *9*, 11151−11159.
(56) Leguy, A. M. A.; Frost, J. M.; McMahon, A. P.; Sakai, V. G.; Kockelmann, W.; Law, C.; Li, X.; Foglia, F.; Walsh, A.; O'Regan, B. C.; et al. The Dynamics of Methylammonium Ions in Hybrid Organic-inorganic Perovskite Solar Cells. *Nat. Commun.* **2015**, *6*, 7124−7126.
(57) Ferreira, A. C.; Paofai, S.; Létoublon, A.; Ollivier, J.; Raymond, S.; Hehlen, B.; Rufflé, B.; Cordier, S.; Katan, C.; Even, J.; et al. Direct Evidence of Weakly Dispersed and Strongly Anharmonic Optical Phonons in Hybrid Perovskites. *Commun. Phys.* **2020**, *3*, 48.
(58) Even, J.; Carignano, M.; Katan, C. Molecular Disorder and Translation/rotation Coupling in the Plastic Crystal Phase of Hybrid Perovskites. *Nanoscale* **2016**, *8*, 6222−6236.
(59) Ehlert, S.; Huniar, U.; Ning, J.; Furness, J. W.; Sun, J.; Kaplan, A. D.; Perdew, J. P.; Brandenburg, J. G. r2SCAN-D4: Dispersion Corrected Meta-generalized Gradient Approximation for General Chemical Applications. *J. Chem. Phys.* **2021**, *154*, 061101.
(60) Bučko, T.; Lebègue, S.; Ángyán, J. G.; Hafner, J. Extending the Applicability of the Tkatchenko-Scheffler Dispersion Correction via Iterative Hirshfeld Partitioning. *J. Chem. Phys.* **2014**, *141*, 034114−034117.
(61) Bokdam, M.; Lahnsteiner, J.; Ramberger, B.; Schäfer, T.; Kresse, G. Assessing Density Functionals Using Many Body Theory for Hybrid Perovskites. *Phys. Rev. Lett.* **2017**, *119*, 145501−145505.
(62) Chi, L.; Swainson, I.; Cranswick, L.; Her, J.-H.; Stephens, P.; Knop, O. The Ordered Phase of Methylammonium Lead Chloride $CH_3ND_3PbCl_3$. *J. Solid State Chem.* **2005**, *178*, 1376−1385.
(63) Lohaus, S. H.; Johnson, M. B.; Ahnn, P. F.; Saunders, C. N.; Smith, H. L.; White, M. A.; Fultz, B. Thermodynamic Stability and

https://doi.org/10.1021/acs.cgd.3c01112
Cryst. Growth Des. 2024, 24, 391−404

Contributions to the Gibbs Free Energy of Nanocrystalline Ni_3Fe. *Phys. Rev. Mater.* **2020**, *4*, 086002−086012.
(64) Sutton, C.; Levchenko, S. V. First-Principles Atomistic Thermodynamics and Configurational Entropy. *Front. Chem.* **2020**, *8*, 1−18.
(65) Esters, M.; Oses, C.; Hicks, D.; Mehl, M. J.; Jahnátek, M.; Hossain, M. D.; Maria, J.-P.; Brenner, D. W.; Toher, C.; Curtarolo, S. Settling the Matter of the Role of Vibrations in the Stability of High-entropy Carbides. *Nat. Commun.* **2021**, *12*, 5747−5811.
(66) Weatherby, J. A.; Rumson, A. F.; Price, A. J. A.; Otero de la Roza, A.; Johnson, E. R. A Density-functional Benchmark of Vibrational Free-energy Corrections for Molecular Crystal Polymorphism. *J. Chem. Phys.* **2022**, *156*, 114108−114110.
(67) Galimberti, D. R.; Sauer, J. Chemically Accurate Vibrational Free Energies of Adsorption from Density Functional Theory Molecular Dynamics: Alkanes in Zeolites. *J. Chem. Theory Comput.* **2021**, *17*, 5849−5862.
(68) Braeckevelt, T.; Goeminne, R.; Vandenhaute, S.; Borgmans, S.; Verstraelen, T.; Steele, J. A.; Roeffaers, M. B. J.; Hofkens, J.; Rogge, S. M. J.; Van Speybroeck, V. Accurately Determining the Phase Transition Temperature of $CsPbI_3$ via Random-Phase Approximation Calculations and Phase-Transferable Machine Learning Potentials. *Chem. Mater.* **2022**, *34*, 8561−8576.
(69) Yang, R. X.; Skelton, J. M.; da Silva, E. L.; Frost, J. M.; Walsh, A. Assessment of Dynamic Structural Instabilities Across 24 Cubic Inorganic Halide Perovskites. *J. Chem. Phys.* **2020**, *152*, 024703.
(70) Otero-de-la-Roza, A.; Johnson, E. R. Application of XDM to Ionic Solids: the Importance of Dispersion for Bulk Moduli and Crystal Geometries. *J. Chem. Phys.* **2020**, *153*, 54121−54211.
(71) Price, A. J. A.; Otero-de-la-Roza, A.; Johnson, E. R. XDM-corrected Hybrid DFT with Numerical Atomic Orbitals Predicts Molecular Crystal Lattice Energies with Unprecedented Accuracy. *Chem. Sci.* **2023**, *14*, 1252−1262.
(72) Williams, R. W.; Heilweil, E. J. Measuring Molecular Force Fields: Terahertz, Inelastic Neutron Scattering, Raman, FTIR, DFT, and BOMD Molecular Dynamics of Solid L-Serine. *Chem. Phys.* **2010**, *373*, 251−260.
(73) Monacelli, L.; Bianco, R.; Cherubini, M.; Calandra, M.; Errea, I.; Mauri, F. The Stochastic Self-consistent Harmonic Approximation: Calculating Vibrational Properties of Materials with Full Quantum and Anharmonic Effects. *J. Phys.: Condens. Matter* **2021**, *33*, 363001−363034.
(74) Carreras, A.; Togo, A.; Tanaka, I. DynaPhoPy: A code for Extracting Phonon Quasiparticles from Molecular Dynamics Simulations. *Comput. Phys. Commun.* **2017**, *221*, 221−234.
(75) Lahnsteiner, J.; Bokdam, M. Anharmonic Lattice Dynamics in Large Thermodynamic Ensembles with Machine-learning Force Fields: $CsPbBr_3$, a Phonon Liquid with Cs Rattlers. *Phys. Rev. B* **2022**, *105*, 024302.
(76) Hellman, O.; Steneteg, P.; Abrikosov, I. A.; Simak, S. I. Temperature Dependent Effective Potential Method for Accurate Free Energy Calculations of Solids. *Phys. Rev. B* **2013**, *87*, 104111.
(77) Liu, Y.; Long, R.; Fang, W.-H.; Prezhdo, O. V. Nuclear Quantum Effects Prolong Charge Carrier Lifetimes in Hybrid Organic−Inorganic Perovskites. *J. Am. Chem. Soc.* **2023**, *145*, 14112−14123.
(78) Monacelli, L.; Marzari, N. First-Principles Thermodynamics of $CsSnI_3$. *Chem. Mater.* **2023**, *35*, 1702−1709.
(79) Kapil, V.; Engel, E. A. A Complete Description of Thermodynamic Stabilities of Molecular Crystals. *Proc. Natl. Acad. Sci. U.S.A.* **2022**, *119*, 21117691199.
(80) Hele, T. J. H. Thermal Quantum Time-correlation Functions from Classical-like Dynamics. *Mol. Phys.* **2017**, *115*, 1435−1462.
(81) Batzner, S.; Musaelian, A.; Sun, L.; Geiger, M.; Mailoa, J. P.; Kornbluth, M.; Molinari, N.; Smidt, T. E.; Kozinsky, B. E(3)-equivariant Graph Neural Networks for Data-efficient and Accurate Interatomic Potentials. *Nat. Commun.* **2022**, *13*, 2453−2511.
(82) Fransson, E.; Rahm, J. M.; Wiktor, J.; Erhart, P. Revealing the Free Energy Landscape of Halide Perovskites: Metastability and Transition Characters in CsPbBr3 and MAPbI3. *Chem. Mater.* **2023**, *35*, 8229−8238.
(83) Chan, Y. T.; Elliger, N.; Klis, B.; Kollár, M.; Horváth, E.; Forró, L.; Dressel, M.; Uykur, E. High-pressure Investigations in $CH_3NH_3PbX_3$ (X = I, Br, and Cl): Suppression of Ion Migration and Stabilization of Low-temperature Structure. *Phys. Rev. B* **2022**, *106*, 214106−214110.
(84) Liang, A.; Gonzalez-Platas, J.; Turnbull, R.; Popescu, C.; Fernandez-Guillen, I.; Abargues, R.; Boix, P. P.; Shi, L.-T.; Errandonea, D. Reassigning the Pressure-Induced Phase Transitions of Methylammonium Lead Bromide Perovskite. *J. Am. Chem. Soc.* **2022**, *144*, 20099−20108.
(85) Jaffe, A.; Lin, Y.; Beavers, C. M.; Voss, J.; Mao, W. L.; Karunadasa, H. I. High-Pressure Single-Crystal Structures of 3D Lead-Halide Hybrid Perovskites and Pressure Effects on their Electronic and Optical Properties. *ACS Cent. Sci.* **2016**, *2*, 201−209.

NOTE ADDED AFTER ASAP PUBLICATION

The missing .zip supporting information file was added December 20, 2023.

https://doi.org/10.1021/acs.cgd.3c01112
Cryst. Growth Des. 2024, 24, 391−404